International Journal of Heat and Mass Transfer 185 (2022) 122348

Contents lists available at ScienceDirect

International Journal of Heat and Mass Transfer

journal homepage: www.elsevier.com/locate/hmt

Theoretical analysis of phase change heat transfer and energy storage in a spherical phase change material with encapsulation

Ankur Jain*, Mohammad Parhizi

Mechanical and Aerospace Engineering Department, University of Texas at Arlington, 500W First St, Rm 211, Arlington, TX 76019, USA

ARTICLE INFO

Article history:
Received 17 August 2021
Revised 2 November 2021
Accepted 28 November 2021

Keywords:
Phase change heat transfer
Encapsulation
Latent energy storage
Melting
Solidification

ABSTRACT

Encapsulation of a phase change material (PCM) is a commonly used technique for providing mechanical and chemical stability, and enabling the manufacturing of PCM composites. However, thermal impedance of the encapsulating layer may adversely affect phase change heat transfer in the PCM. Experimental measurement of heat transfer and phase change in an encapsulated PCM is difficult, particularly for the case of micro/nano-encapsulation. As a result, development of robust theoretical phase change heat transfer models in presence of encapsulation is critical. This paper presents theoretical analysis of the problem of phase change heat transfer in a spherical PCM with an encapsulant layer. Temperature distribution in the newly formed phase and the encapsulant layer is determined by solving a spherical two-layer thermal conduction problem in non-dimensional form. The rate of phase change propagation is then determined from the temperature distribution. The effect of thermal contact resistance at the PCM-encapsulant interface is accounted for. Results are shown to be consistent with past work for the special case of no encapsulation. Results are also shown to agree well with numerical simulations. The use of only a few eigenvalues is shown to result in good accuracy. The effect of encapsulant thickness, thermal properties and PCM-encapsulant thermal contact resistance as well as external boundary condition on phase change propagation is analyzed. The non-dimensional model is used to address practical problems in phase change energy storage with typical materials and conditions. This work contributes an important theoretical analysis tool for a problem of much practical importance. Results from this work may help optimize and improve the performance of encapsulated PCMs for energy storage and thermal management.

1. Introduction

Phase change materials (PCMs) are commonly used for energy storage in a variety of engineering systems, including in storing energy from intermittent sources such as solar energy [1]. Phase change offers much greater energy storage density compared to sensible storage due to the large latent heat of PCMs [2]. A large body of literature already exists on a variety of aspects of energy storage in PCMs, including materials [3], heat transfer enhancement [4], theoretical heat transfer modeling and optimization [5], and system-level implementation [6].

PCMs are often encapsulated within a thin layer of another material that does not undergo phase change [7]. Encapsulation prevents the melted PCM from flowing away, and also enables the manufacturing of PCM composites [8]. PCM encapsulation has been carried out at the macroscale, as well as at micro/nano scales. While micro/nano-encapsulation is more complicated to manufacture, it offers enhanced surface area and therefore more effective heat transfer to/from the ambient [7]. Common encapsulant materials include polymers such as Polymethyl methacrylate (PMMA) [1] and Polyester [9], and metals in both bulk [10] and nanoparticle form [11]. Experimental investigation of the impact of shell thickness relative to core radius has been reported [10,12,13], and a trade-off between mechanical stability and thermal characteristics (rate and amount of heat stored) has been identified. The volume shrinkage method has been used to measure the extent of solidification as a function of time in a spherical encapsulated PCM [14], although this approach requires insertion of a descending tube into the spherical PCM, and, therefore, is unlikely to be practical for micro/nanoscale PCM. In general, direct experimental measurement of temperature and phase change front in an encapsulated PCM is difficult due to lack of optical access and difficulties in insertion of a sensor into a micro/nano-sized PCM [8]. While thermal properties of the encapsulant have been identified as playing a key role in determining heat transfer and phase change in the composite [7], nevertheless, there is a lack of systematic investigation of this im-

* Corresponding author.
E-mail address: jaina@uta.edu (A. Jain).

https://doi.org/10.1016/j.ijheatmasstransfer.2021.122348
0017-9310/

Nomenclature

Bi	Biot number, $Bi = hR_0/k_L$
C	heat capacity ($Jkg^{-1}K^{-1}$)
$\bar{g}$	non-dimensional thermal contact resistance at the PCM-encapsulant interface, $\bar{g} = R_{e-L}k_L/R_0$
$\mathcal{L}$	latent heat of phase change (Jkg^{-1})
$\bar{k}_e$	non-dimensional thermal conductivity of encapsulant ($\bar{k}_e = k_e/k_L$)
k	thermal conductivity ($Wm^{-1}K^{-1}$)
h	convective heat transfer coefficient ($Wm^{-2}K^{-1}$)
r	radial coordinate (m)
R_0	radius of the PCM (m)
R_{e-L}	thermal contact resistance at the PCM-encapsulant interface (Km^2W^{-1})
Ste	Stefan number, $Ste = C(T_0 - T_m)/\mathcal{L}$
T_0	ambient temperature (K)
T	temperature field (K)
T_m	PCM melting temperature (K)
x_{LS}	location of phase change front, measured inwards from the PCM outer surface (m)
$\bar{\alpha}_e$	non-dimensional thermal diffusivity of encapsulant, $\bar{\alpha}_e = \alpha_e/\alpha_L$
α	thermal diffusivity (m^2s^{-1})
δ	encapsulant thickness (m)
$\bar{\delta}$	non-dimensional encapsulant thickness, $\bar{\delta} = \delta/R_0$
ξ	non-dimensional spatial coordinate, $\xi = \frac{r}{R_0}$
ξ_{LS}	non-dimensional location of phase change front, $\xi_{LS} = x_{LS}/R_0$
τ	non-dimensional time, $\tau = \alpha_L t/R_0^2$
θ	non-dimensional temperature, $\theta_i = (T_i - T_m)/(T_0 - T_m)$, $i = L$, e

Subscripts

full	complete melting
L	liquid PCM
e	encapsulant
in	initial temperature

portant aspect, likely due to difficulties in measurement of thermal properties and *in situ* heat transfer across the encapsulant.

Given the difficulties in direct heat transfer measurements in a PCM-encapsulant composite, theoretical modeling of phase change heat transfer in a PCM-encapsulant composite is very important. As a baseline, a large body of literature exists on modeling of phase change of a spherical PCM without encapsulation. Approximate solutions for inward phase change in a sphere have been derived using various techniques such as perturbation method [15] and heat-balance integral method [16], strained coordinates method [17,18], matched asymptotic expansions method [19] and an iterative technique [20]. A singularity has been identified when the phase change front reaches the center of the sphere [16,18]. A number of papers have also reported numerical computation of the inward propagation of phase change in a sphere [21–23]. Most of these papers utilize the enthalpy method for numerical computations.

In contrast with the literature on phase change in a homogeneous spherical PCM, a limited amount of work has been reported on heat transfer modeling in the presence of an encapsulating layer. Due to the additional complexity introduced by the presence of the encapsulant, most of such work utilizes numerical simulations instead of analytical modeling. For example, numerical simulations to account for convection in the liquid phase and close contact melting have been carried out and compared with experimental measurements [24]. Multi-mode heat transfer simulation of an encapsulated PCM has been reported [25]. Numerical calculations have been carried out to understand the impact of material properties and geometry on phase change process in a PCM-encapsulant composite [26]. A moving grid technique has been used to numerically solve this problem for a PCM-encapsulant composite, and the effect of encapsulant thickness on the phase change process has been reported [27]. The encapsulant has been modeled as a thermal resistance by neglecting the transient temperature gradient that may exist within the encapsulant [28]. Such an approach is likely to break down when the encapsulant is thick and/or has low thermal diffusivity. Despite the availability of such numerical models, development of robust theoretical models remains very desirable. In contrast with numerical simulations, analytical models offer a more general and universal understanding. In particular, theoretical models may help develop generalized relationships between non-dimensional parameters to describe the effect of encapsulant thickness and thermal properties, and the interplay between material parameters and other process parameters such as the convective heat transfer coefficient on the outer surface. Understanding the effect of encapsulant thickness is of particular interest, as a thick encapsulant increases conduction heat transfer resistance, but also increases the surface area available for convective heat transfer from the ambient. Theoretical modeling may also help understand the effect of thermal contact resistance at the PCM-encapsulant interface, which has not been addressed in the past work, but may be important in solidification problems where the encapsulant may be in imperfect thermal contact with the solid PCM. While an exhaustive number of papers have presented theoretical analysis of the problem of phase change in a homogeneous sphere, as summarized above, there remains a lack of theoretical analysis of phase change in a PCM-encapsulant composite, where the thickness and thermal properties of the encapsulant, as well as thermal contact resistance at the PCM-encapsulant interface may play a key role in determining the nature of phase change propagation.

This paper presents an analytical model for predicting the temperature distribution and propagation of the phase change front during phase change in a spherical PCM-encapsulant composite. The analytical model accounts for interfacial thermal resistance between the PCM and encapsulant, as well as convective boundary conditions on the outer surface of the composite. The temperature field is solved by considering thermal conduction in a two-layer spherical geometry comprising the encapsulant and melted PCM, following which, an expression for the location of the phase change front is derived. While this is an approximate analytical solution, good accuracy is expected, particularly for small values of the Stefan number. The effect of encapsulant thickness and thermal properties on the PCM melting process is investigated using the model. The key novelty of the present work is in the development of an analytical solution for the phase change heat transfer problem in a spherical core-shell composite, for which, past literature only offers numerical simulations. In addition to improving the theoretical understanding of phase change heat transfer, this work also contributes towards the design and optimization of encapsulated PCM for practical latent heat storage systems.

2. Problem definition

A schematic of the problem considered here is presented in Fig. 1. A spherical phase change material of radius R_0 is encapsulated by a thickness δ of a material that does not undergo phase change. The specific interest here is in a micro-encapsulated PCM, in which, the PCM size is small enough that convective effects can be neglected and heat transfer can be assumed to occur only through thermal conduction. Considering the melting problem, this

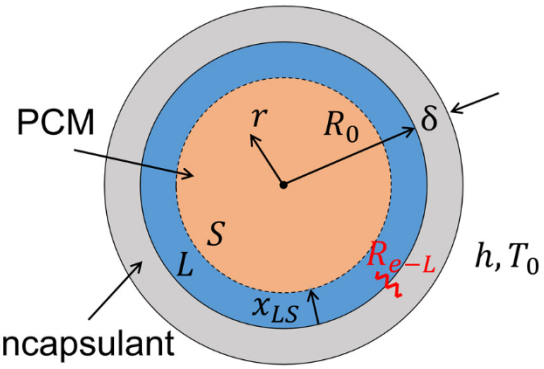

Fig. 1. Schematic geometry of the problem considered here: A spherical phase change material (PCM) is encapsulated by a non-phase change layer, and the composite is subjected to convection from a high temperature on the outer surface. A thermal contact resistance is assumed between the two layers.

core-shell composite receives heat from the ambient at temperature T_0 through convective heat transfer on the outer surface, with a convective heat transfer coefficient h. This results in gradual melting of the PCM and inward propagation of the phase change front until all the PCM has melted. The PCM is assumed to be initially a solid at the melting temperature, T_m. The location of the phase change front at any time, $x_{LS}(t)$ is shown in Fig. 1, and is measured inwards from the outer surface of the PCM core. Thermal conductivity and diffusivity are denoted by k and α. Heat capacity and latent heat of phase change are denoted by C and $\mathcal{L}$, respectively. A thermal contact resistance $R_{e\text{-}L}$ – defined as the ratio between temperature difference and heat flux at the interface – is assumed at the PCM-encapsulant interface. Subscripts L and e refer to the newly melted liquid phase and encapsulant, respectively. Volumetric expansion/contraction due to phase change is ignored, since the density of liquid and solid phases of several PCMs are close to each other. Natural convection in the liquid phase is neglected. All properties are assumed to be independent of temperature. The two key performance parameters of interest include x_{LS} as a function of time, and the total time taken from complete melting. While the problem discussed here is that of melting, similar analysis can be carried out for solidification as well as equivalent mass transfer problems.

This problem can be described mathematically by the following differential equations:

$$\frac{1}{r^2}\frac{\partial}{\partial r}\left(r^2\frac{\partial T_L}{\partial r}\right)=\frac{1}{\alpha_L}\frac{\partial T_L}{\partial t}\quad (x_{LS}<r<R_0) \tag{1}$$

$$\frac{1}{r^2}\frac{\partial}{\partial r}\left(r^2\frac{\partial T_e}{\partial r}\right)=\frac{1}{\alpha_e}\frac{\partial T_e}{\partial t}\quad (R_0<r<R_0+\delta) \tag{2}$$

In addition, the following conditions must be satisfied

$$T_L=T_m\quad (r=R_0-x_{LS}) \tag{3}$$

$$k_e\frac{\partial T_e}{\partial r}=h(T_0-T_e)\quad (r=R_0+\delta) \tag{4}$$

Eq. (3) arises from the phase change that occurs at $r=R_0-x_{LS}$, whereas Eq. (4) represents the convective heat transfer boundary condition on the outer surface of the core-shell composite. Note that, as shown in Fig. 1, x_{LS} is measured inwards from the PCM-encapsulant interface, so that $x_{LS}=0$ at $t=0$.

At the liquid-encapsulant interface, $r=R_0$, the following conditions must be satisfied

$$T_e=T_L+R_{e-L}k_L\frac{\partial T_L}{\partial r}\quad (r=R_0) \tag{5}$$

$$k_e\frac{\partial T_e}{\partial r}=k_L\frac{\partial T_L}{\partial r}\quad (r=R_0) \tag{6}$$

Note that Eq. (5) follows from the definition of the interfacial thermal contact resistance as the ratio of the temperature difference and heat flux at the interface. An interfacial thermal contact resistance arises due to imperfect geometrical contact between the two materials at the interface [29], and/or due to phonon scattering at the interface due to acoustic mismatch [30]. Interfacial thermal contact resistance is common in layered engineering systems [31,32], and has been accounted for in the present work for generality. In the case of perfect thermal contact between the PCM and encapsulant, the value of R_{e-L} can be simply set to zero.

The initial temperature of the encapsulant is taken to be $T_e(r,0)=T_{e,in}(r)$. Finally, energy conservation at the phase change interface can be used to write the following relationship between the rate of phase change front propagation and the temperature field:

$$\rho_L\mathcal{L}\frac{dx_{LS}}{dt}=k_L\left(\frac{\partial T_L}{\partial r}\right)_{r=R_0-x_{LS}} \tag{7}$$

It is helpful to non-dimensionalize this problem in order to ensure generality of the results. The following non-dimensional terms are introduced: $\xi=\frac{r}{R_0}$, $\tau=\frac{\alpha_L t}{R_0^2}$, $\theta_e=\frac{T_e-T_m}{T_0-T_m}$, $\theta_L=\frac{T_L-T_m}{T_0-T_m}$, $\xi_{LS}=x_{LS}/R_0$, $\bar{\alpha}_e=\alpha_e/\alpha_L$, $\bar{k}_e=k_e/k_L$, $\bar{\delta}=\delta/R_0$, $\bar{g}=R_{e-L}k_L/R_0$; $Bi=hR_0/k_L$. This results in the following set of non-dimensional equations for the liquid and encapsulant temperature fields and the phase change front location, $\xi_{LS}(\tau)$

$$\frac{1}{\xi^2}\frac{\partial}{\partial\xi}\left(\xi^2\frac{\partial\theta_L}{\partial\xi}\right)=\frac{\partial\theta_L}{\partial\tau}\quad (\xi_{LS}<\xi<1) \tag{8}$$

$$\frac{1}{\xi^2}\frac{\partial}{\partial\xi}\left(\xi^2\frac{\partial\theta_e}{\partial\xi}\right)=\frac{1}{\bar{\alpha}_e}\frac{\partial\theta_e}{\partial\tau}\quad \left(1<\xi<1+\bar{\delta}\right) \tag{9}$$

$$\theta_L=0\quad (\xi=1-\xi_{LS}) \tag{10}$$

$$-\bar{k}_e\frac{\partial\theta_e}{\partial r}=Bi(\theta_e-1)\quad \left(\xi=1+\bar{\delta}\right) \tag{11}$$

$$\theta_e=\theta_L+\bar{g}\frac{\partial\theta_L}{\partial\xi}\quad (\xi=1) \tag{12}$$

$$\bar{k}_e\frac{\partial\theta_e}{\partial\xi}=\frac{\partial\theta_L}{\partial\xi}\quad (\xi=1) \tag{13}$$

$$\frac{d\xi_{LS}}{d\tau}=Ste\left(\frac{\partial\theta_L}{\partial\xi}\right)_{\xi=1-\xi_{LS}} \tag{14}$$

The non-dimensional problem represented by Eqs. (8)–(13) can be solved by the method of eigenfunction expansion. Since the phase change front itself changes with time, the resulting solution is not exact, but reasonable accuracy is expected at small Ste. Due to the presence of a non-homogeneous term in the boundary condition at $\xi=1+\bar{\delta}$ (Eq. (11)), one must first write the solution as a sum of two components as follows

$$\theta_L(\xi,\tau)=u_L(\xi)+w_L(\xi,\tau) \tag{15}$$

$$\theta_e(\xi,\tau)=u_e(\xi)+w_e(\xi,\tau) \tag{16}$$

where u_L and u_e satisfy $(\xi^2u_L')'=0$ and $(\xi^2u_e')'=0$, respectively. Boundary conditions satisfied by u_L and u_e are

$$u_L=0\quad (\xi=1-\xi_{LS}) \tag{17}$$

$$-\bar{k}_e u_e' = Bi(u_e - 1) \quad \left(\xi = 1 + \bar{\delta}\right) \tag{18}$$

$$u_e = u_L + \bar{g} u_L' \quad (\xi = 1) \tag{19}$$

$$\bar{k}_e u_e' = u_L' \quad (\xi = 1) \tag{20}$$

A solution for $u_L(\xi)$ and $u_e(\xi)$ can be easily found to be

$$u_L(\xi) = \frac{-\bar{k}_e Bi}{-Bi\left(\frac{1}{1+\bar{\delta}} + \bar{m}\right) + \frac{\bar{k}_e}{(1+\bar{\delta})^2}} \left(\frac{1}{\xi} - \frac{1}{1-\xi_{LS}}\right) \tag{21}$$

$$u_e(\xi) = \frac{-Bi}{-Bi\left(\frac{1}{1+\bar{\delta}} + \bar{m}\right) + \frac{\bar{k}_e}{(1+\bar{\delta})^2}} \left(\bar{m} + \frac{1}{\xi}\right) \tag{22}$$

where

$$\bar{m} = \bar{k}_e\left(1 - \bar{g} - \frac{1}{1-\xi_{LS}}\right) - 1 \tag{23}$$

Once $u_L(\xi)$ and $u_e(\xi)$ are determined, the problem for $w_L(\xi, \tau)$ and $w_e(\xi, \tau)$ may be written as

$$\frac{1}{\xi^2}\frac{\partial}{\partial \xi}\left(\xi^2 \frac{\partial w_L}{\partial \xi}\right) = \frac{\partial w_L}{\partial \tau} \quad (\xi_{LS} < \xi < 1) \tag{24}$$

$$\frac{1}{\xi^2}\frac{\partial}{\partial \xi}\left(\xi^2 \frac{\partial w_e}{\partial \xi}\right) = \frac{1}{\bar{\alpha}_e}\frac{\partial w_e}{\partial \tau} \quad \left(1 < \xi < 1 + \bar{\delta}\right) \tag{25}$$

$$w_L = 0 \quad (\xi = 1 - \xi_{LS}) \tag{26}$$

$$-\bar{k}_e \frac{\partial w_e}{\partial r} = Bi \cdot w_e \quad \left(\xi = 1 + \bar{\delta}\right) \tag{27}$$

$$w_e = w_L + \bar{g}\frac{\partial w_L}{\partial \xi} \quad (\xi = 1) \tag{28}$$

$$\bar{k}_e \frac{\partial w_e}{\partial \xi} = \frac{\partial w_L}{\partial \xi} \quad (\xi = 1) \tag{29}$$

The initial conditions for this problem are

$$w_e = \theta_{e,in}(\xi) - u_e(\xi) \quad (\tau = 0) \tag{30}$$

$$w_L = -u_L(\xi) \quad (\tau = 0) \tag{31}$$

where $\theta_{e,in}(\xi) = \frac{T_{e,in}(r) - T_m}{T_0 - T_m}$. The boundary conditions of this problem are now homogeneous, and therefore, one may write the solution in terms of the usual eigenfunctions for a spherical body as follows:

$$w_e(\xi, \tau) = \sum_{n=1}^{\infty}\left[\frac{A_{1,n}}{\xi}\cos\left(\frac{\lambda_n\left(\xi - \left(1+\bar{\delta}\right)\right)}{\sqrt{\bar{\alpha}_e}}\right) + \frac{B_{1,n}}{\xi}\sin\left(\frac{\lambda_n\left(\xi - \left(1+\bar{\delta}\right)\right)}{\sqrt{\bar{\alpha}_e}}\right)\right]\exp\left(-\lambda_n^2\tau\right) \tag{32}$$

$$w_L(\xi, \tau) = \sum_{n=1}^{\infty}\left[\frac{A_{2,n}}{\xi}\cos\left(\lambda_n(\xi - (1-\xi_{LS}))\right) + \frac{B_{2,n}}{\xi}\sin\left(\lambda_n(\xi - (1-\xi_{LS}))\right)\right]\exp\left(-\lambda_n^2\tau\right) \tag{33}$$

Based on the boundary condition at $\xi = 1 - \xi_{LS}$, Eq. (26), one must choose $A_{2,n} = 0$. Further, from Eq. (27), one may find that $A_{1,n} = s_n B_{1,n}$, where

$$s_n = \frac{\bar{k}_e \lambda_n}{\sqrt{\bar{\alpha}_e}\left(-Bi + \frac{\bar{k}_e}{(1+\bar{\delta})}\right)} \tag{34}$$

Further, the interface conditions at $\xi = 1$ results in

$$B_{1,n}\left[s_n \cos\left(\frac{\lambda_n\bar{\delta}}{\sqrt{\bar{\alpha}_e}}\right) - \sin\left(\frac{\lambda_n\bar{\delta}}{\sqrt{\bar{\alpha}_e}}\right)\right] = B_{2,n}[\sin(\lambda_n\xi_{LS}) + \bar{g}(-\sin(\lambda_n\xi_{LS}) + \lambda_n\cos(\lambda_n\xi_{LS}))] \tag{35}$$

$$\bar{k}_e B_{1,n}\left[-s_n\cos\left(\frac{\lambda_n\bar{\delta}}{\sqrt{\bar{\alpha}_e}}\right) + \frac{s_n\lambda_n}{\sqrt{\bar{\alpha}_e}}\sin\left(\frac{\lambda_n\bar{\delta}}{\sqrt{\bar{\alpha}_e}}\right) + \sin\left(\frac{\lambda_n\bar{\delta}}{\sqrt{\bar{\alpha}_e}}\right) + \frac{\lambda_n}{\sqrt{\bar{\alpha}_e}}\cos\left(\frac{\lambda_n\bar{\delta}}{\sqrt{\bar{\alpha}_e}}\right)\right] = B_{2,n}[-\sin(\lambda_n\xi_{LS}) + \lambda_n\cos(\lambda_n\xi_{LS})] \tag{36}$$

Dividing Eqs. (35) by (36) results in the following eigenequation for this problem

$$-\bar{k}_e\left[1 + \frac{\lambda_n}{\sqrt{\bar{\alpha}_e}}\frac{\cot\left(\frac{\lambda_n\bar{\delta}}{\sqrt{\bar{\alpha}_e}}\right) + s_n}{1 - s_n\cot\left(\frac{\lambda_n\bar{\delta}}{\sqrt{\bar{\alpha}_e}}\right)}\right] = \frac{\lambda_n\cot(\lambda_n\xi_{LS}) - 1}{1 + \bar{g}(\lambda_n\cot(\lambda_n\xi_{LS}) - 1)} \tag{37}$$

Thus, the solution may be written as

$$w_e(\xi, \tau) = \sum_{n=1}^{\infty} B_{1n}\left[\frac{s_n}{\xi}\cos\left(\frac{\lambda_n\left(\xi - \left(1+\bar{\delta}\right)\right)}{\sqrt{\bar{\alpha}_e}}\right) + \frac{1}{\xi}\sin\left(\frac{\lambda_n\left(\xi - \left(1+\bar{\delta}\right)\right)}{\sqrt{\bar{\alpha}_e}}\right)\right]\exp\left(-\lambda_n^2\tau\right) \tag{38}$$

$$w_L(\xi, \tau) = \sum_{n=1}^{\infty}\frac{-B_{1n}p_n}{\xi}\sin(\lambda_n(\xi - (1-\xi_{LS})))\exp\left(-\lambda_n^2\tau\right) \tag{39}$$

where, from Eq. (35),

$$p_n = \frac{-s_n\cos\left(\frac{\lambda_n\bar{\delta}}{\sqrt{\bar{\alpha}_e}}\right) + \sin\left(\frac{\lambda_n\bar{\delta}}{\sqrt{\bar{\alpha}_e}}\right)}{\sin(\lambda_n\xi_{LS}) + \bar{g}(-\sin(\lambda_n\xi_{LS}) + \lambda_n\cos(\lambda_n\xi_{LS}))} \tag{40}$$

Finally, the initial condition is used to determine the last remaining unknown coefficient, B_{1n}. Inserting $\tau = 0$ in Eqs. (38) and (39) and using Eqs. (30) and (31), one may obtain

$$\theta_{e,in}(\xi) - u_e(\xi) = \sum_{n=1}^{\infty} B_{1n}\left[\frac{s_n}{\xi}\cos\left(\frac{\lambda_n\left(\xi - \left(1+\bar{\delta}\right)\right)}{\sqrt{\bar{\alpha}_e}}\right) + \frac{1}{\xi}\sin\left(\frac{\lambda_n\left(\xi - \left(1+\bar{\delta}\right)\right)}{\sqrt{\bar{\alpha}_e}}\right)\right] \tag{41}$$

$$-u_L(\xi) = \sum_{n=1}^{\infty}\frac{-B_{1n}p_n}{\xi}\sin(\lambda_n(\xi - (1-\xi_{LS}))) \tag{42}$$

Multiplying Eqs. (41) and (42) by $\frac{\bar{k}_e}{\bar{\alpha}_e}\xi^2\left[\frac{s_m}{\xi}\cos\left(\frac{\lambda_m(\xi-(1+\bar{\delta}))}{\sqrt{\bar{\alpha}_e}}\right) + \frac{1}{\xi}\sin\left(\frac{\lambda_m(\xi-(1+\bar{\delta}))}{\sqrt{\bar{\alpha}_e}}\right)\right]$ and $\frac{-p_m}{\xi}\xi^2\sin(\lambda_m(\xi - (1-\xi_{LS})))$, respectively, integrating and adding,

one may obtain, using the principle of orthogonality of eigenfunctions [33]

$$B_{1m} = \frac{1}{N_m}\left[\frac{\bar{k}_e}{\bar{\alpha}_e}\int_1^{1+\bar{\delta}}[\theta_{e,in}(\xi)-u_e(\xi)]\xi^2\left[\frac{s_m}{\xi}\cos\left(\frac{\lambda_m\left(\xi-\left(1+\bar{\delta}\right)\right)}{\sqrt{\bar{\alpha}_e}}\right)+\frac{1}{\xi}\sin\left(\frac{\lambda_m\left(\xi-\left(1+\bar{\delta}\right)\right)}{\sqrt{\bar{\alpha}_e}}\right)\right]d\xi + \int_{1-\xi_{LS}}^{1} u_L(\xi)\frac{p_m}{\xi}\xi^2\sin\left(\lambda_m(\xi-(1-\xi_{LS}))\right)d\xi\right] \tag{43}$$

where the norm N_m is given by

$$N_m = \frac{\bar{k}_e}{\bar{\alpha}_e}\int_1^{1+\bar{\delta}}\xi^2\left[\frac{s_m}{\xi}\cos\left(\frac{\lambda_m\left(\xi-\left(1+\bar{\delta}\right)\right)}{\sqrt{\bar{\alpha}_e}}\right)+\frac{1}{\xi}\sin\left(\frac{\lambda_m\left(\xi-\left(1+\bar{\delta}\right)\right)}{\sqrt{\bar{\alpha}_e}}\right)\right]^2 d\xi + \int_{1-\xi_{LS}}^{1}\xi^2\left[\frac{p_m}{\xi}\sin\left(\lambda_m(\xi-(1-\xi_{LS}))\right)\right]^2 d\xi \tag{44}$$

which completes the solution for the temperature distribution. Finally, the phase change front may be obtained by inserting Eqs. (21) and (39) into Eq. (14), resulting in

$$\frac{d\xi_{LS}}{d\tau} = Ste\left[\frac{\bar{k}_e Bi}{-Bi\left(\frac{1}{1+\bar{\delta}}+\bar{m}\right)+\frac{\bar{k}_e}{\left(1+\bar{\delta}\right)^2}}\cdot\frac{1}{\left(1-\xi_{LS}\right)^2} + \sum_{n=1}^{\infty}-\frac{B_{1n}p_n\lambda_n}{1-\xi_{LS}}\exp\left(-\lambda_n^2\tau\right)\right] \tag{45}$$

where ξ_{LS} is zero at the initial time.

Note that the u_L and u_e components of the solution represent the quasi-steady solution that neglects transient effects in the encapsulant.

3. Special cases

The solution derived in Section 2 assumes a general convective boundary condition on the outer surface of the core-shell composite. A special case of particular interest is that of isothermal conditions on the outer surface, which may occur in case of a heat source of large thermal mass. The results in this case may be obtained from the general results presented in Section 2 by setting $Bi \to \infty$. This leads to much simplification, including $s_n = 0$. $u_e(\xi)$ and $u_L(\xi)$ are given by

$$u_L(\xi) = \bar{k}_e\left(\frac{\frac{1}{\xi}-\frac{1}{1-\xi_{LS}}}{\bar{m}+\frac{1}{1+\bar{\delta}}}\right) \tag{46}$$

$$u_e(\xi) = \frac{\bar{m}+\frac{1}{\xi}}{\bar{m}+\frac{1}{1+\bar{\delta}}} \tag{47}$$

The solution for $w_e(\xi,\tau)$ is given by

$$w_e(\xi,\tau) = \sum_{n=1}^{\infty}\frac{B_{1n}}{\xi}\sin\left(\frac{\lambda_n\left(\xi-\left(1+\bar{\delta}\right)\right)}{\sqrt{\bar{\alpha}_e}}\right)\exp\left(-\lambda_n^2\tau\right) \tag{48}$$

$w_L(\xi,\tau)$ continues to be given by Eq. (39), with the simplified definition of $p_n = \frac{\sin\left(\frac{\lambda_n\bar{\delta}}{\sqrt{\bar{\alpha}_e}}\right)}{\sin(\lambda_n\xi_{LS})+\bar{g}(-\sin(\lambda_n\xi_{LS})+\lambda_n\cos(\lambda_n\xi_{LS}))}$. The eigenequation is still given by Eq. 37 with $s_n = 0$. The coefficients B_{1m} are given by

$$B_{1m} = \frac{1}{N_m}\left[\frac{\bar{k}_e}{\bar{\alpha}_e}\int_1^{1+\bar{\delta}}[\theta_{e,in}(\xi)-u_e(\xi)]\xi\sin\left(\frac{\lambda_m\left(\xi-\left(1+\bar{\delta}\right)\right)}{\sqrt{\bar{\alpha}_e}}\right)d\xi + \int_{1-\xi_{LS}}^{1}u_L(\xi)p_m\xi\sin^2(\lambda_m(\xi-(1-\xi_{LS})))d\xi\right] \tag{49}$$

where

$$N_m = \frac{\bar{k}_e}{\bar{\alpha}_e}\int_1^{1+\bar{\delta}}\sin^2\left(\frac{\lambda_m\left(\xi-\left(1+\bar{\delta}\right)\right)}{\sqrt{\bar{\alpha}_e}}\right)d\xi + \int_{1-\xi_{LS}}^{1}[p_m\sin(\lambda_m(\xi-(1-\xi_{LS})))]^2 d\xi \tag{50}$$

Finally, an expression to determine the phase change front is given by

$$\frac{d\xi_{LS}}{d\tau} = Ste\left[\frac{-\bar{k}_e}{\frac{1}{1+\bar{\delta}}-\left(1+\bar{k}_e\frac{\bar{g}+\xi_{LS}-\bar{g}\xi_{LS}}{1-\xi_{LS}}\right)}\cdot\frac{1}{\left(1-\xi_{LS}\right)^2} + \sum_{n=1}^{\infty}-\frac{c_n p_n\lambda_n}{1-\xi_{LS}}\exp\left(-\lambda_n^2\tau\right)\right] \tag{51}$$

The case of perfect thermal contact between the PCM and encapsulant may also be of interest in practical applications. In such a case, the solution may be further simplified by setting $\bar{g} = 0$ in equations above, resulting in further simplification.

4. Results and discussion

4.1. Verification

The infinite series solutions presented in Sections 2 and 3 must be truncated to a finite number of terms for computation. It is important to verify the convergence of the series solution and to determine the minimum number of terms needed for series convergence. Towards this, the phase change front as a function of time is computed for a representative problem for different number of eigenvalues considered in the series solution. For $\bar{k}_e = 0.5, \bar{\alpha}_e = 0.5, Ste = 0.1$, $\bar{g} = 1$, Fig. 2(a) and (b) present these plots for two different encapsulant thicknesses, $\bar{\delta} = 0.4$ and $\bar{\delta} = 2.0$, respectively. For the first case, Fig. 2(a) shows convergence of the series solution within a single term. The inclusion of further terms does not significantly impact the accuracy of the solution. This is likely because when the encapsulant is very thin, transient thermal gradients within the encapsulant are negligible, and even the zero eigenvalue case shown in Fig. 2(a), which corresponds to the quasi-steady solution is sufficient. On the other hand, when the encapsulant is quite thick, such as $\bar{\delta} = 2.0$ shown in Fig. 2(b), the quasi-steady technique is clearly in error, and a greater number of terms are needed for series convergence. Even in this case, however, just a few terms in the series are sufficient. The rapid convergence of the series solution is helpful for minimizing computational cost. Up to $\bar{\delta} = 0.5$ or $\bar{\delta} = 1.0$, it is found that the single-term solution results in errors of 0.1% and 0.7%, respectively, in prediction of the time taken for full melting, with other parameter values listed above.

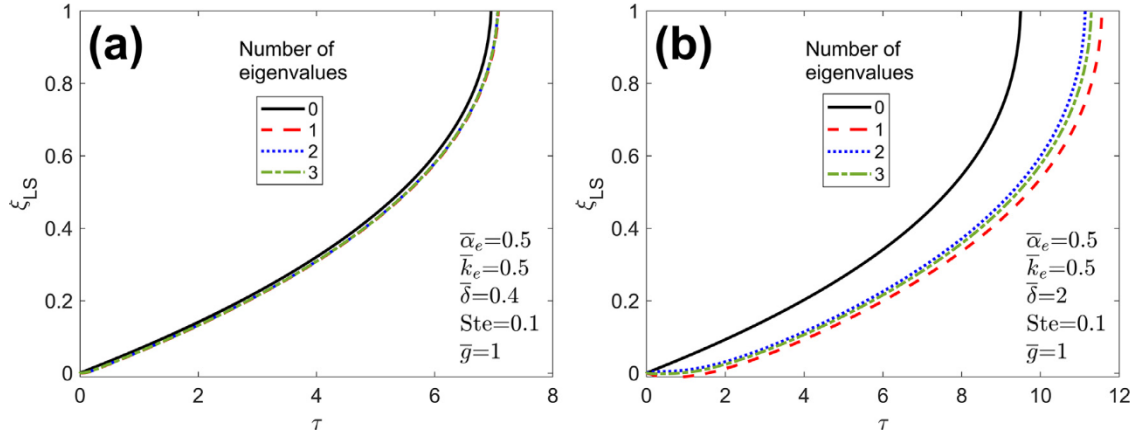

Fig. 2. Effect of number of eigenvalues: Phase change propagation front as a function of time for melting of an encapsulated PCM with different number of eigenvalues considered in Eq. (45). The case of zero eigenvalues, representing the quasi-steady solution is also included. The encapsulant thicknesses are (a) $\bar{\delta} = 0.4$, (b) $\bar{\delta} = 2.0$. Values of other parameters are $\bar{k}_e = 0.5; \bar{\alpha}_e = 0.5; Ste = 0.1; \bar{g} = 1$.

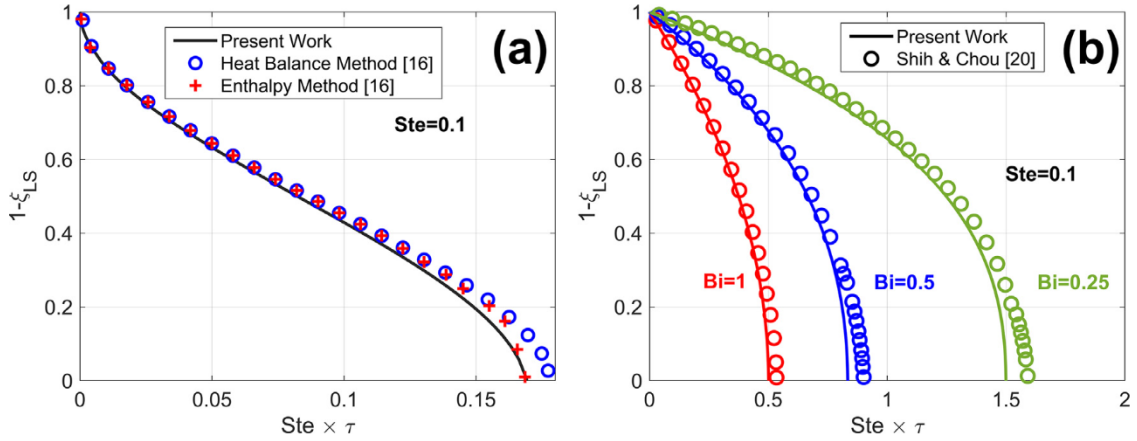

Fig. 3. Comparison with past work for a homogeneous spherical PCM: Phase change propagation as a function of time for $Ste = 0.1$, showing results from present work with very thin encapsulant, $\bar{\delta} = 0.001$ for the case of (a) isothermal boundary condition, presented by Caldwell and Chan [16], and (b) convective boundary condition, presented by Shih and Chou [20].

Note that ξ_{LS} shown in Fig. 2 (and subsequent Figures) is measured radially inwards, which is why ξ_{LS} is zero at the initial time, and grows as time passes.

A number of papers in the past have analyzed the problem of inward phase change in a sphere without an encapsulant [15–19,21–23]. For this special case, two comparisons of the present work with past papers are carried out. The first comparison pertains to an isothermal boundary condition, $Bi \to \infty$, for which, an approximate solution based on the heat balance integral method [34] and enthalpy method has been presented by Caldwell and Chan [16]. These results are compared with the present model, computed with a very thin encapsulant, $\bar{\delta} = 0.001$, in Fig. 3(a). Consistent with Caldwell and Chan [16], the value of Stefan number is taken to be $Ste = 0.1$. Results show very good agreement between the present work and results presented by Caldwell and Chan, particularly with the enthalpy method. The melting front propagates rapidly at first, due to being close to the hot boundary, then slows down due to increasing distance from the hot boundary, and finally speeds up towards the end of the process when very little solid PCM remains. There is some disagreement at the end, which is consistent with the singularity that is known to exist at the center, $\xi = 1.0$ in this problem [16]. Note that the error in each approximate method may contribute towards the overall deviation shown in Fig. 3. Further note that, consistent with the past work [16], the x and y axes in Fig. 3 plot $Ste \cdot \tau$, and the phase change propagation front measured from the center, $1 - \xi_{LS}$, respectively.

The second comparison pertains to the case of a finite Biot number that represents a convective boundary condition. For this case, comparison is carried out with Shih and Chou [20], who solved this problem for a homogeneous spherical PCM using an iterative analytical technique. For $Ste = 0.1$, and with three different values of Bi, Fig. 3(b) presents comparison of the present work with Shih and Chou [20]. Similar to the previous comparison, a small value of encapsulant thickness, $\bar{\delta} = 0.001$ is used in order to enable a reasonable comparison. Fig. 3(b) shows very good agreement between the past work and the present model at each value of Bi for which data are available from the past work. The comparison presented in Fig. 3 for the special case of a pure PCM sphere by modeling a very thin encapsulant layer provides confidence in the present model. Note that comparison with past work has been presented in non-dimensional form, and therefore, does not depend on the specific PCMs that may have been considered in the past papers.

For further verification of the theoretical model presented here, results for a representative problem are compared against numerical simulations. The numerical simulation is carried out using a variable timestep implicit finite difference method. The governing equations for both encapsulant and PCM are discretized in space with equal intervals, Δx. The timestep is determined via numer-

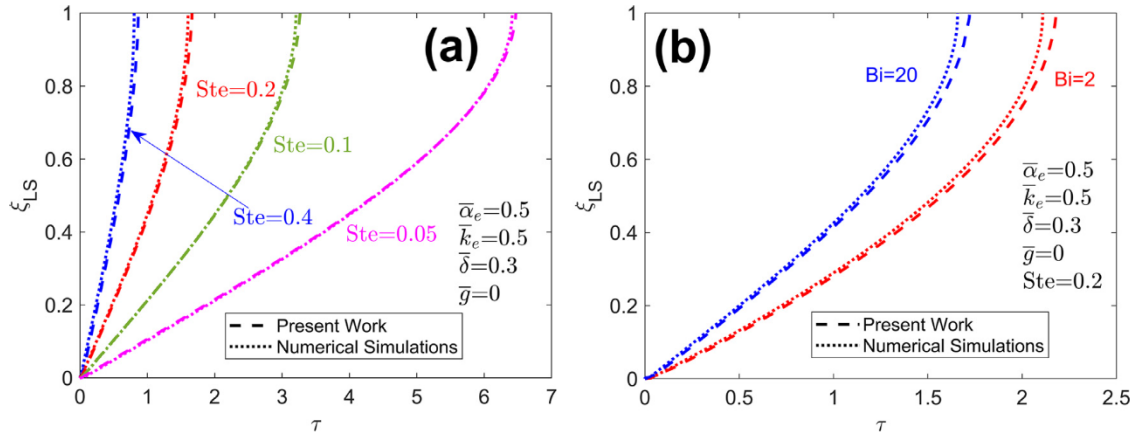

Fig. 4. Comparison of present work with finite-difference numerical simulations: Phase change propagation front as a function of time for the present work and a finite-difference based numerical computation. (a) Comparison for four different values of *Ste* with isothermal boundary condition; (b) Comparison for convective boundary condition with two different values of *Bi* , assuming $Ste = 0.2$. Values of other parameters are $\bar{k}_e = 0.5; \bar{\alpha}_e = 0.5; \bar{\delta} = 0.3; \bar{g} = 0$.

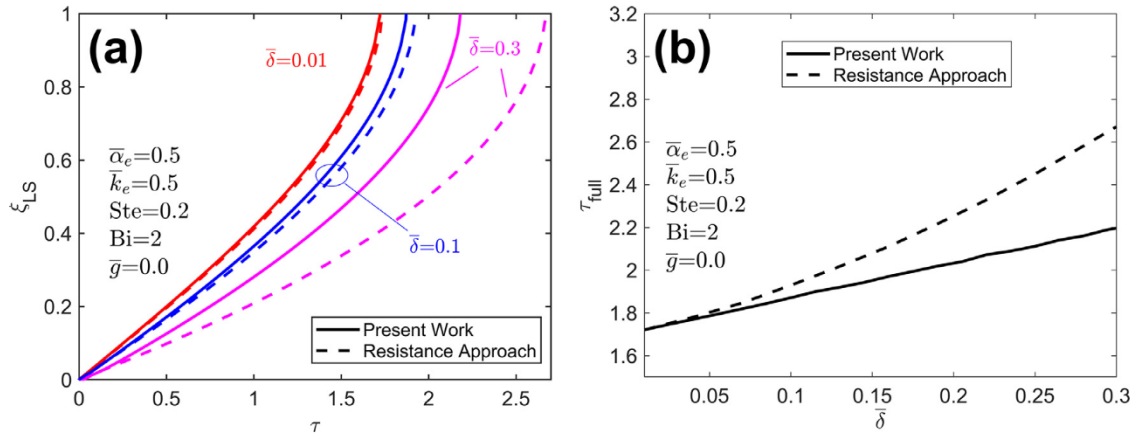

Fig. 5. Comparison of present work with resistance technique to account for encapsulant: (a) Phase change propagation front as a function of time for different values of $\bar{\delta}$. (b) Time for complete melting as a function of $\bar{\delta}$ for the present work and resistance approach. Curves based on present work and resistance approach are both plotted. Values of other parameters are $\bar{k}_e = 0.5; \bar{\alpha}_e = 0.5; Ste = 0.2; Bi = 2; \bar{g} = 0$.

ical iteration in such a way that the phase change front moves by Δx during that time. Continuity of temperature and heat flux is applied on the node at the encapsulant-PCM interface. 1000 nodes are found to be sufficient for mesh-independent results for this one-dimensional problem. For the case of isothermal boundary, Fig. 4(a) presents the phase change propagation plot, showing results from the present work as well as numerical simulations for four different values of *Ste*. In this and all subsequent Figures, the encapsulant is assumed to initially be at the melting temperature, similar to the PCM itself, which is a realistic assumption. Other problem parameters are $\bar{k}_e = 0.5; \bar{\alpha}_e = 0.5; \bar{\delta} = 0.3;\ \bar{g} = 0$. Fig. 4(a) shows excellent agreement between the two for each *Ste*. A similar comparison is presented for a more general convective boundary condition in Fig. 4(b). In this case, the comparison is presented for two different values of *Bi*, with $\bar{k}_e = 0.5; \bar{\alpha}_e = 0.5; \bar{\delta} = 0.3;\ \bar{g} = 0.0; Ste = 0.2$. In both cases, there is very good agreement between the present work and numerical simulations. This provides additional confidence in the present model.

It is also instructive to compare the present work with an approximate technique that has been proposed in past work to account for the presence of the encapsulant. For the case of a thin encapsulant, its impact on the melting process has been modeled by adding its thermal resistance to the convective resistance at the boundary, and subsequently ignoring the encapsulant completely [28]. This approach does not account for transient thermal gradients and sensible heat storage in the encapsulant. A derivation of the phase change front location as a function of time based on this assumption is presented in Supplementary Information. Fig. 5 compares the predictions of the present model with the resistance approach. The phase change front predicted by the two approaches is plotted in Fig. 5(a) as a function of time for three different values of the encapsulant thicknesses – $\bar{\delta} = 0.01,\ 0.1,\ 0.3$. Values of other parameters are $\bar{k}_e = 0.5; \bar{\alpha}_e = 0.5; Ste = 0.2; Bi = 2; \bar{g} = 0$. Fig. 5(a) shows that for $\bar{\delta} = 0.01$, the resistance approach is in good agreement with the present work. This is expected because when the encapsulant is very thin, it does not store significant sensible heat, and may be accurately modeled as a thermal resistance. However, as the encapsulant thickness increases, the resistance approach is less and less accurate, while the present approach correctly accounts for transient thermal conduction within the encapsulant. At $\bar{\delta} = 0.3$, Fig. 5(a) shows significant error in the resistance approach discussed in past work [28]. To further illustrate this comparison, the total time taken for melting, τ_{full} is plotted in Fig. 5(b) as a function of encapsulant thickness, $\bar{\delta}$ for the present work and the resistance approach. At small encapsulant thicknesses, the two are in reasonable agreement. However, as the encapsulant thickness increases, the resistance approach predicts increasingly inaccurate τ_{full} because as the encapsulant thickness increases, thermal diffusion takes longer and longer, and sensible heat storage is also greater, which has been completely ignored in the resistance ap-

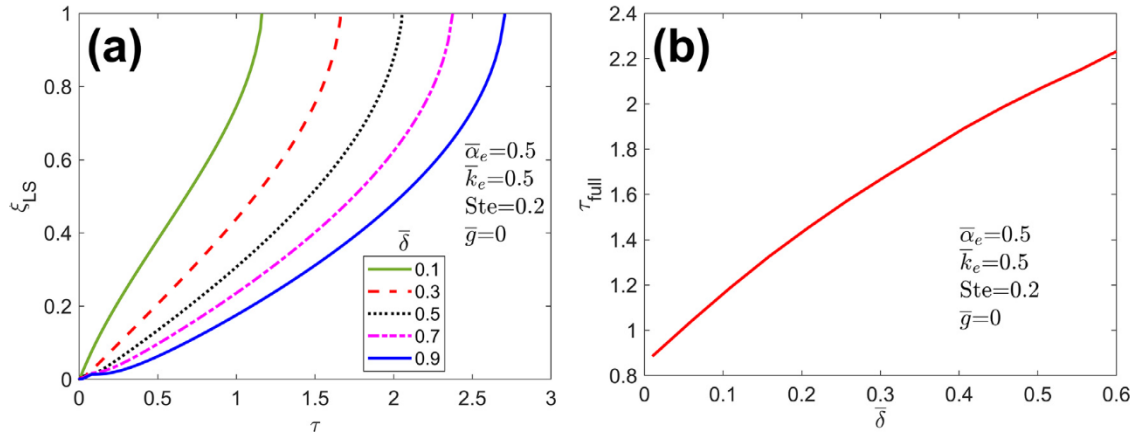

Fig. 6. Effect of encapsulant thickness, $\bar{\delta}$: Phase change propagation front as a function of time for different values of $\bar{\delta}$; (b) Time for complete melting as a function of $\bar{\delta}$. Values of other parameters are $\bar{k}_e = 0.5; \bar{\alpha}_e = 0.5; Ste = 0.2; \bar{g} = 0$.

proach. By accounting for these factors through a transient diffusion analysis of the PCM-encapsulant composite, the present work results in more reasonable prediction of the melting process.

4.2. Effect of encapsulant thickness

The impact of the encapsulant thickness is further illustrated in Fig. 6. A thick encapsulant is usually preferred for mechanical stability [7]. However, this might reduce the rate of melting, and thus, the amount of energy stored. In order to understand this important trade-off, the phase change front is plotted as a function of time for several values of the encapsulant thickness and with $\bar{k}_e = 0.5; \bar{\alpha}_e = 0.5; Ste = 0.2$. Perfect thermal contact and isothermal external boundary condition are assumed. Fig. 6(a) illustrates several key features of the melting curve. As $\bar{\delta}$ increases, melting occurs slower and slower. The physical reason behind this is the increased time taken for diffusion through the encapsulant layer. As the phase change front proceeds inwards, melting occurs faster, which is opposite to the well-known slowdown of the melting process in a Cartesian one-dimensional phase change problem due to the increasing thermal impedance of the newly melted layer. The reason behind this is that in a spherical geometry, as the melting front moves inwards, the volume of the remaining PCM decreases rapidly (due to r^3 dependence of volume in a sphere). This results in rapid increase in the rate of melting towards the end, as shown in Fig. 6(a). As the melting process reaches completion, $\xi_{LS} \rightarrow 1$, the rate of melting is, in principle, infinite. For practical computation of the problem, the time step is needed to be reduced in order to accurately capture the rising rate of melting as the process approaches completion. The increase in the rate of melting towards the end of inwards spherical phase change has been noted in past papers [15,16,28]. In addition, the singularity existing as $\xi_{LS} \rightarrow 1$ has also been recognized in past work [16,18].

Fig. 6(b) presents the time taken for complete melting as a function of the encapsulant thickness. As expected, a thicker encapsulant results in larger τ_{full}. This is because of the increased time needed for diffusion through the encapsulant before PCM melting can occur. Note that the rate of melting becomes increasingly large as the process approaches completion, which is why, in these calculations, τ_{full} is approximated by extrapolation between last two points on the $\tau - \xi_{LS}$ curve once ξ_{LS} reaches a value of 0.99. This may result in slight error in the predicted value of τ_{full}. Alternately, the melting characteristics of the core-shell composite may be represented by the time taken to complete a certain fraction, say 95%, of the total melting process, thereby avoiding the singularity at the end of the process.

4.3. Effect of Stefan number

In practical applications, the impact of external temperature is also important to understand. The Stefan number, *Ste*, is the key non-dimensional parameter that represents the magnitude of the external heat source. In order to understand the effect of *Ste* on the melting process, the phase change front ξ_{LS} is computed as a function of τ for four different values of *Ste*. An encapsulant thickness of $\bar{\delta}$=0.2 is assumed. Other properties are $\bar{k}_e = 0.6; \bar{\alpha}_e = 0.4;\ \bar{g} = 0$. The external boundary condition is taken to be isothermal, i.e., $Bi \rightarrow \infty$. Plots presented in Fig. 7(a) show, as expected, that increasing *Ste* results in more rapid rate of melting, particularly in the initial stages of melting. This is due to greater amount of heat conducted through the encapsulant and newly melted PCM. A plot of the time taken for full melting as a function of *Ste* is shown in Fig. 7(b). This plot shows that as *Ste* is reduced starting from a large value, τ_{full} first increases slowly, and then rises very rapidly as *Ste* becomes smaller and smaller. This is in contrast with the nearly linear dependence of τ_{full} on encapsulant thickness $\bar{\delta}$ shown in Fig. 6(b).

4.4. Effect of interfacial thermal contact resistance

The analytical models presented in Sections 2 and 3 explicitly account for thermal contact resistance at the PCM-encapsulant interface. While perfect thermal contact between the two has often been assumed in past work, interfacial thermal contact resistance may exist between the two due to surface roughness or due to a more fundamental mismatch in acoustic velocities between the two, resulting in phonon scattering at the interface. Moreover, in the case of solidification process, the newly solidified PCM may not be in perfect contact with the encapsulant due to surface roughness or other reasons. Therefore, it is important to understand the impact of thermal contact resistance on the phase change process. Fig. 8(a) plots the melting curve for different values of $\bar{g}$, including $\bar{g} = 0$ that corresponds to perfect thermal contact. As expected, Fig. 8(a) shows that thermal contact resistance between PCM and encapsulant results in reduced rate of melting, represented by the slope of the melting curve, especially at early times. This is attributable to reduced heat flow across the interface due to the thermal contact resistance. While the slopes of the curves are quite similar at large times, it takes longer for the melting front to reach the center of the sphere as $\bar{g}$ increases due to the increased resistance to flow of heat at the interface. It is instructive to plot the temperature distributions in the PCM-encapsulant composite to further understand the impact of $\bar{g}$. These are plotted in Fig. 8(b)

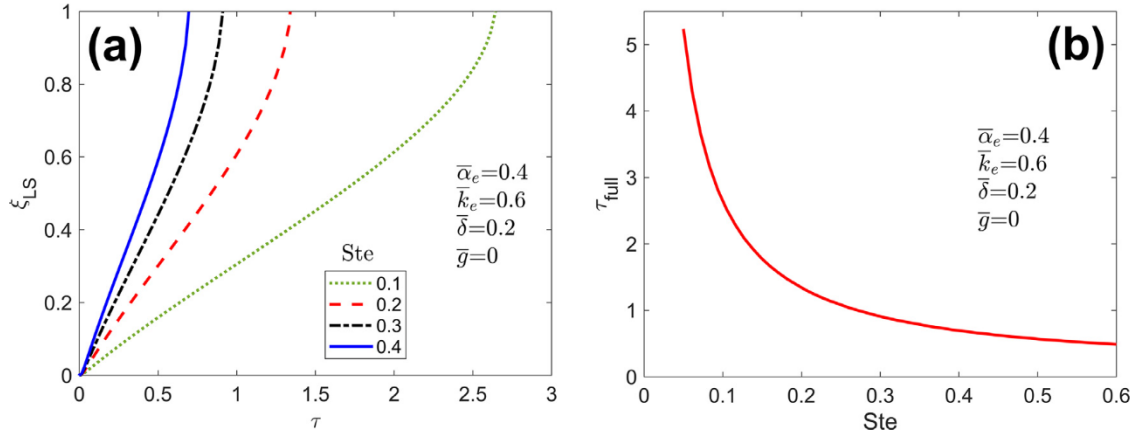

Fig. 7. Effect of Stefan number: Phase change propagation front as a function of time for different values of *Ste*; (b) Time for complete melting as a function of *Ste*. Values of other parameters are $\bar{k}_e = 0.6; \bar{\alpha}_e = 0.4; \bar{\delta} = 0.2; \bar{g} = 0$.

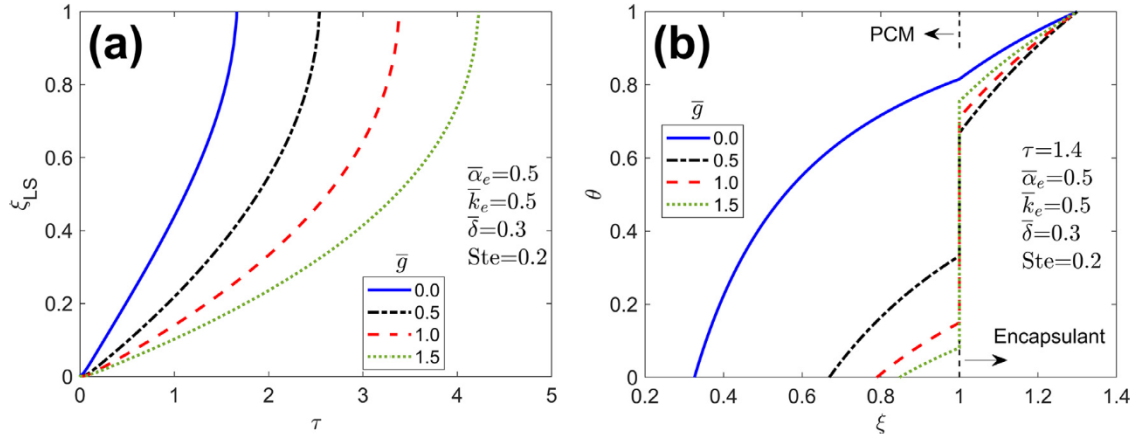

Fig. 8. Effect of interfacial contact resistance: Phase change propagation front as a function of time for different values of $\bar{g}$; (b) Temperature distribution in the PCM-encapsulant composite at τ=1.4 for different values of $\bar{g}$. Values of other parameters are $\bar{k}_e = 0.5; \bar{\alpha}_e = 0.5; \bar{\delta} = 0.3; Ste = 0.2$.

at a fixed time, $\tau = 1.4$. For $\bar{g} = 0$, a continuous temperature profile is observed in Fig. 8(b). The presence of thermal contact resistance is seen to result in a discontinuity at the PCM-encapsulant interface, the magnitude of which increases with $\bar{g}$. This results in lower and lower penetration of the temperature field into the PCM as well as reduced slope of the temperature distribution at the phase change front. This explains the reduction in rate of melting due to thermal contact resistance, as seen in Fig. 8(a), because the slope of this curve is directly responsible for determining the rate of propagation of the phase change front (Eq. (45)). A practical aspect of the thermal contact resistance is to understand its impact on the time taken for complete melting. This is plotted in Fig. 9 for $\bar{k}_e = 0.5; \bar{\alpha}_e = 0.5; \bar{\delta} = 0.3; Ste = 0.2$ and isothermal external boundary condition. Fig. 9 offers useful design guidelines for practical energy storage systems where thermal contact resistance may be encountered.

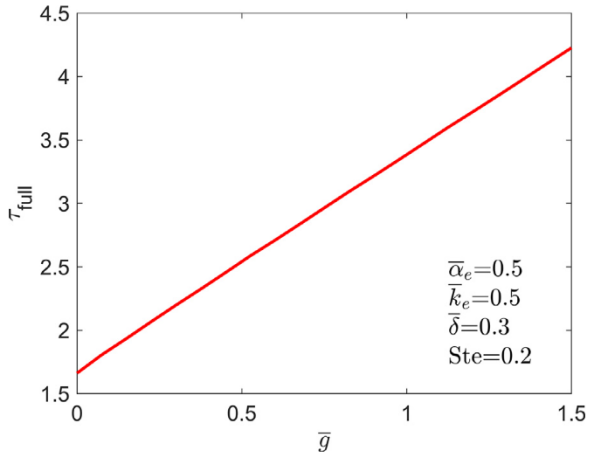

Fig. 9. Effect of interfacial contact resistance: Time for complete melting as a function of $\bar{g}$. Values of other parameters are $\bar{k}_e = 0.5; \bar{\alpha}_e = 0.5; \bar{\delta} = 0.3; Ste = 0.2$.

4.5. Effect of Biot number

Convective conditions on the outer surface of the core-shell composite may also influence the melting and energy storage processes. This is represented by the non-dimensional Biot number. $Bi = 0$ corresponds to adiabatic conditions, which is not of interest for the present work. On the other hand, $Bi \to \infty$ renders the boundary isothermal, results for which are discussed as a special case in Section 3. In order to understand the impact of the convective boundary condition on the melting process, Fig. 10(a) plots the melting curve for multiple values of *Bi*, including the isothermal special case. Values of various parameters for Fig. 10(a) are $\bar{k}_e = 0.5; \bar{\alpha}_e = 0.5; \bar{g} = 0; \ \bar{\delta} = 0.4$. Fig. 10(a) shows that strong convection on the outer surface results in rapid melting. This is mainly due to increased rate of heat transfer into the encapsulant layer. As *Bi* increases, the curves approach the separately calculated curve for the isothermal special case (Eq. (51)). Fig. 10(a) shows that

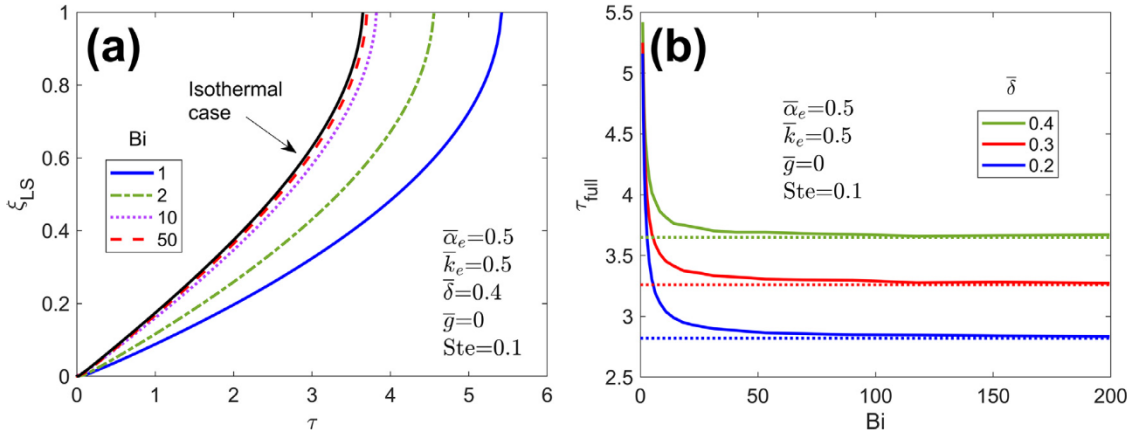

Fig. 10. Effect of Biot number: (a) Phase change propagation front as a function of time for different values of *Bi* with $\bar{\delta} = 0.4$; (b) Time for complete melting as a function of *Bi* for three different values of encapsulant thicknesses. The isothermal curve and isothermal values of τ_{full} are also indicated in (a) and (b), respectively. Values of other parameters are $\bar{k}_e = 0.5; \bar{\alpha}_e = 0.5; \bar{g} = 0$.

$Bi = 50$ is nearly identical to the isothermal curve. To further investigate this, Fig. 10(b) plots the time taken for full melting as a function of *Bi* for three different values of encapsulant thickness $\bar{\delta}$. In each case, the time taken for full melting reduces as *Bi* increases (i.e., as one moves towards isothermal conditions). This is mainly due to increased rate of heat transfer from the ambient into the PCM-encapsulant composite. The asymptotic value of τ_{full} at large *Bi* matches well with the value expected from isothermal analysis (Section 3), shown in Fig. 10(b) using dotted lines for each thickness. Fig. 10(b) also shows that τ_{full} asymptotes to a larger value for thicker encapsulant, which is reasonable because the larger the encapsulant thickness, the lower is the rate of heat flow into the encapsulant, and thus, the larger is the time taken for full melting.

4.6. Practical applications

The theoretical model presented in Sections 2 and 3 is next applied to characterize the performance of a practical PCM-encapsulant composite. In realistic applications, it is of much interest to determine the time taken for full melting and its dependence on various parameters such as encapsulant thickness and ambient temperature. Experimental measurement of these relationships is cumbersome, and therefore, theoretical predictions may be helpful in guiding such experiments, as well as in designing practical energy storage systems.

For this investigation, the PCM and encapsulant are assumed to be octadecane and PMMA, respectively, which have been investigated widely in the literature for phase change energy storage. Previously reported thermal properties for these materials are used [5,35]. PCM radius of 50 μm – typical of micro-encapsulated PCMs [8] – is taken.

First, the impact of encapsulant thickness on time taken for melting is investigated. The external source is assumed to be 20 K above melting temperature. Perfect thermal contact at the PCM-encapsulant interface and isothermal conditions at the external boundary are assumed. Based on these assumptions, Fig. 11 plots the predicted plot of time taken for full melting as a function of encapsulant thickness ranging from 0.5 to 25 μm (1 to 50% of PCM radius). This Figure is plotted in dimensional form. As expected, as the encapsulant thickness increases, it takes longer and longer for the PCM to fully melt. Under similar assumptions as the previous Figure, the effect of external source temperature on the melting process is shown in Fig. 12. Here, the encapsulant thickness is assumed to be 10 μm. Fig. 12 shows that as the ambient temperature increases, melting occurs faster and faster.

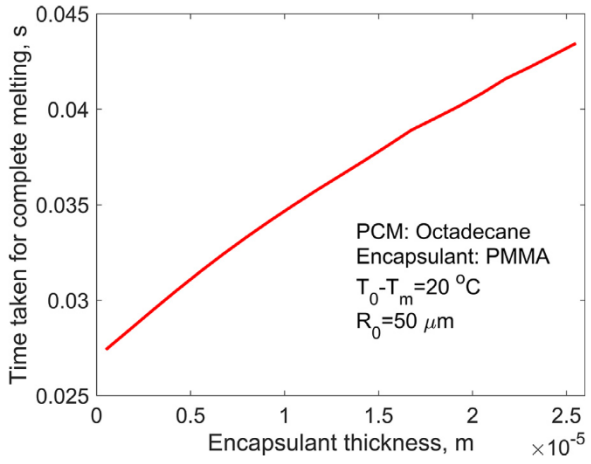

Fig. 11. Application of the model for a practical problem: Melt time as a function of encapsulant thickness for 50 μm PCM radius. Properties of octadecane and PMMA are assumed for PCM and encapsulant, respectively. Perfect thermal contact at the interface is assumed. The hot source is assumed to be 20 K above melting temperature with isothermal conditions on the outer surface and perfect thermal contact between PCM and encapsulant.

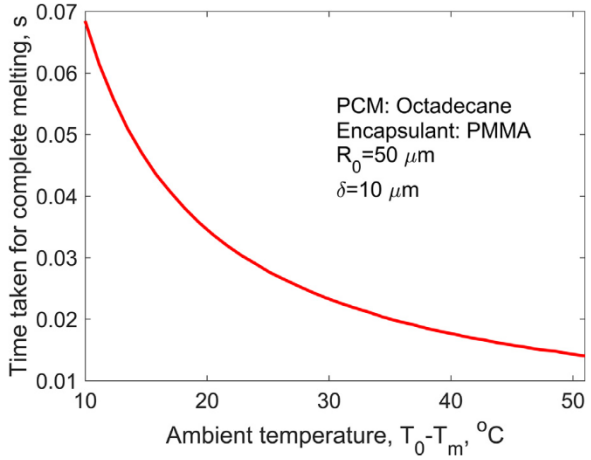

Fig. 12. Application of the model for a practical problem: Melt time as a function of the hot source temperature. Properties of octadecane and PMMA are assumed for PCM and encapsulant, respectively. PCM radius and encapsulant thickness are 50 μm and 10 μm, respectively. Perfect thermal contact at the interface and isothermal boundary condition are assumed.

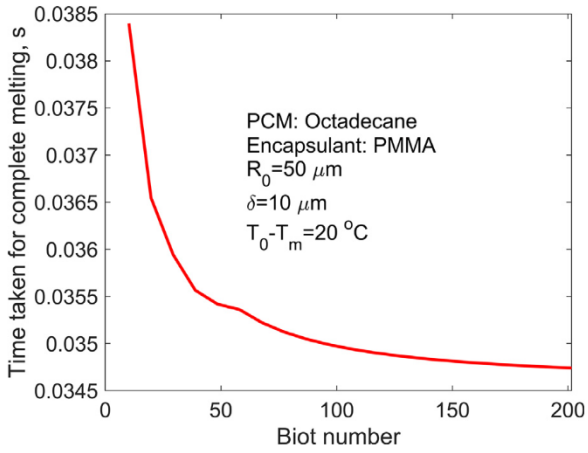

Fig. 13. Application of the model for a practical problem: Melt time as a function of the convective heat transfer coefficient at the outer boundary. Properties of octadecane and PMMA are assumed for PCM and encapsulant, respectively. PCM radius and encapsulant thickness are 50 μm and 10 μm, respectively. Ambient is assumed to be 20 K above melting temperature.

Finally, Fig. 13 plots the impact of the external convective heat transfer coefficient on the time taken for melting. By implementing a convective boundary condition instead of isothermal (as assumed in Figs. 11–13) shows that as h increases, the time taken for melting reduces. This is because a higher value of h corresponds to more effective heat transfer from the ambient into the PCM-encapsulant composite. This effect saturates at high values of h – beyond a threshold, there is no significant incremental benefit in further improving h since the extent of heat transfer is already very close to the best-case isothermal condition.

Dimensional figures such as ones discussed here provide practical guidelines for the design of phase change energy storage systems. While presented for one specific PCM-encapsulant pair, the generalized non-dimensional analysis presented in this work can be easily adapted for any other material system of interest.

5. Conclusion

While encapsulation of phase change materials is a commonly used technique for improving phase change energy storage, *in situ* measurement of heat transfer and phase change in the presence of an encapsulant is very difficult. As a result, theoretical heat transfer models, such as one presented here may play an important role in determining the impact of parameters such as encapsulant thickness, encapsulant thermal properties, as well as external boundary conditions. This may help reduce experimental work needed to optimize the PCM-encapsulant composite towards enhanced phase change energy storage.

While several theoretical models for phase change in a homogeneous PCM sphere are available in the literature, this work accounts for the presence of an encapsulant, thereby offering a more accurate model, particularly when the encapsulant is relatively thick and/or has relatively low diffusivity. Results are derived in this work in non-dimensional form, and therefore, are universally applicable to a broad range of materials and geometries, as long as the underlying assumptions continue to be satisfied.

It is important to recognize the key limitations of the present work. The PCM size must be small enough to be able to neglect natural convection within the liquid phase. In a microencapsulated PCM, which is the focus of the present work, the Grashof number is usually small enough to justify this assumption. Thermal transport properties must be independent of temperature, which is also reasonable when temperature differences in the problem are small. Volume change during phase change is neglected, which is a reasonable assumption for a variety of PCMs.

This work contributes towards theoretical understanding of PCM encapsulation, and may help design and optimize practical phase change energy storage systems.

Declaration of Competing Interest

The authors declare that they have no known competing financial interests or personal relationships that could have appeared to influence the work reported in this paper.

CRediT authorship contribution statement

Ankur Jain: Conceptualization, Methodology, Formal analysis, Investigation, Data curation, Supervision, Project administration, Writing – original draft, Writing – review & editing. **Mohammad Parhizi:** Conceptualization, Methodology, Investigation, Validation, Data curation, Writing – original draft, Writing – review & editing.

Acknowledgments

This material is based upon work supported by CAREER Award No. CBET-1554183 from the National Science Foundation.

Supplementary materials

Supplementary material associated with this article can be found, in the online version, at doi:10.1016/j.ijheatmasstransfer.2021.122348.

References

[1] A. Sari, C. Alkan, A. Karaipekli, O. Uzun, Microencapsulated n-octacosane as phase change material for thermal energy storage, Sol. Energy 83 (2009) 1757–1763.
[2] A. Alexiades, Mathematical Modeling of Melting and Freezing Processes, CRC Press, 1992.
[3] A. Sharma, V.V. Tyagi, C.R. Chen, D. Buddhi, Review on thermal energy storage with phase change materials and applications, Renew. Sustain. Energy Rev. 13 (2009) 318–345.
[4] P. Sivasamy, A. Devaraju, S. Harikrishnan, Review on heat transfer enhancement of phase change materials (PCMs), Mater. Today Proc. 5 (2018) 14423–14431.
[5] A. Mostafavi, M. Parhizi, A. Jain, Theoretical modeling and optimization of fin-based enhancement of heat transfer into a phase change material, Int. J. Heat Mass Transf. 145 (2019) 118698:1–10.
[6] B. Zalba, J.M. Marín, L.F. Cabeza, H. Mehling, Review on thermal energy storage with phase change: materials, heat transfer analysis and applications, Appl. Therm. Eng. 23 (2003) 251–283.
[7] P.B. Salunkhe, P.S. Shembekar, A review on effect of phase change material encapsulation on the thermal performance of a system, Renew. Sustain. Energy Rev. 16 (2012) 5603–5616.
[8] M.N.A. Hawlader, M.S. Uddin, M.M. Khin, Microencapsulated PCM thermal-energy storage system, Appl. Energy 74 (2003) 195–202.
[9] A.S. Lee, Phase Change Materials in Floor Tiles For Thermal Energy Storage, Colorado State University, USA, 2005 Ph.D. Thesis.
[10] J. Wei, Y. Kawaguchi, S. Hirano, H. Takeuchi, Study on a PCM heat storage system for rapid heat supply, Appl. Therm. Eng. 25 (2005) 2903–2920.
[11] Q. Song, Y. Li, J. Xing, J.Y. Hu, Y. Marcus, Thermal stability of composite phase change material microcapsules incorporated with silver nano-particles, Polymer 48 (2007) 3317–3323.
[12] J. Su, L. Ren, L. Wang, Preparation and mechanical properties of thermal energy storage microcapsules, Colloid Polym. Sci. 284 (2005) 224–228.
[13] S.K. Roy, S. Sengupta, An evaluation of phase change microcapsules for use in enhanced heat transfer fluids, Int. Commun. Heat Transf. 18 (1991) 495–507.
[14] M.J. Liu, L.W. Fan, Z.Q. Zhu, F. Feng, H.C. Zhang, Y. Zeng, A volume-shrinkage-based method for quantifying the inward solidification heat transfer of a phase change material filled in spherical capsules, Appl. Therm. Eng. 108 (2016) 1200–1205.
[15] R.I. Pedroso, G.A. Domoto, Perturbation solutions for spherical solidification of saturated liquids, ASME J. Heat Transf. 95 (1973) 42–46.
[16] J. Caldwell, C.C. Chan, Spherical solidification by the enthalpy method and the heat balance integral method, Appl. Math. Model. 24 (2000) 45–53.
[17] M. Prud'homme, T.H. Nguyen, D.L. Nguyen, A heat transfer analysis for solidification of slabs, cylinders, and spheres, ASME J. Heat Transf. 111 (1989) 699–705.

[18] R.I. Pedroso, G.A. Domoto, Inward spherical solidification-solution by the method of strained coordinates, Int. J. Heat Mass Transf. 16 (1973) 1037–1043.
[19] D.S. Riley, S.T. Smith, G. Poots, The inward solidification of spheres and circular cylinders, Int. J. Heat Mass Transf. 17 (1974) 1507–1516.
[20] Y.P. Shih, T.C. Chou, Analytical solutions for freezing a saturated liquid inside or outside spheres, Chem. Eng. Sci. 26 (1971) 1787–1793.
[21] L.C. Tao, Generalized numerical solutions of freezing a saturated liquid in cylinders and spheres, AIChE J. 13 (1967) 165.
[22] P.M. Beckett, Problems Involving Heat Transfer with Change of Phase, Hull University, United Kingdom, 1971 Ph.D. Thesis.
[23] L. Bilir, Z. İlken, Total solidification time of a liquid phase change material enclosed in cylindrical/spherical containers, Appl. Therm. Eng. 25 (2005) 1488–1502.
[24] E. Assis, L. Katsman, G. Ziskind, Numerical and experimental study of melting in a spherical shell, Int. J. Heat Mass Transf. 50 (2007) 1790–1804.
[25] A.R. Archibold, M.M. Rahman, D.Y. Goswami, E.K. Stefanakos, Analysis of heat transfer and fluid flow during melting inside a spherical container for thermal energy storage, Appl. Therm. Eng. 64 (2014) 394–407.
[26] W. Zhao, Characterization of Encapsulated Phase Change Materials For Thermal Energy Storage, Lehigh University, USA, 2013 Ph.D. Thesis.
[27] K.A.R. Ismail, J.R. Henrıq́uez, Solidification of PCM inside a spherical capsule, Energy Convers. Manag. 41 (2000) 173–187.
[28] K.A.R. Ismail, R.I.R. Moraes, A numerical and experimental investigation of different containers and PCM options for cold storage modular units for domestic applications, Int. J. Heat Mass Transf. 52 (2009) 4195–4202.
[29] M.G. Cooper, B.B. Mikic, M.M. Yovanovich, Thermal contact conductance, Int. J. Heat Mass Transf. 12 (1969) 279–300.
[30] E.T. Swartz, R.O. Pohl, Thermal boundary resistance, Rev. Mod. Phys. 61 (1989) 505.
[31] V. Vishwakarma, C. Waghela, Z. Wei, R. Prasher, S.C. Nagpure, J. Li, F. Liu, C. Daniel, A. Jain, Heat transfer enhancement in a lithium-ion cell through improved material-level thermal transport, J. Power Sources 300 (2015) 123–131.
[32] S. Kaur, N. Raravikar, B.A. Helms, R. Prasher, D.F. Ogletree, Enhanced thermal transport at covalently functionalized carbon nanotube array interfaces, Nat. Commun. 5 (2014) 1–8.
[33] M.D. Mikhailov, M.N. Özışık, Unified Analysis and Solutions of Heat and Mass Diffusion, John Wiley & Sons, New York, 1984.
[34] T.R. Goodman, The heat balance integral and its application to problems involving a change of phase, Trans. ASME 80 (1958) 335–342.
[35] http://www.goodfellow.com/E/Polymethylmethacrylate.html, last accessed July 19, 2021.